nature materials

ARTICLES

https://doi.org/10.1038/s41563-020-0729-1

Glassy Li metal anode for high-performance rechargeable Li batteries

Xuefeng Wang[1,5], Gorakh Pawar[2,5], Yejing Li[1], Xiaodi Ren[3], Minghao Zhang[1], Bingyu Lu[1], Abhik Banerjee[1], Ping Liu[1], Eric J. Dufek[4], Ji-Guang Zhang[3], Jie Xiao[3], Jun Liu[3], Ying Shirley Meng[1]✉ and Boryann Liaw[4]✉

Lithium metal has been considered an ideal anode for high-energy rechargeable Li batteries, although its nucleation and growth process remains mysterious, especially at the nanoscale. Here, cryogenic transmission electron microscopy was used to reveal the evolving nanostructure of Li metal deposits at various transient states in the nucleation and growth process, in which a disorder–order phase transition was observed as a function of current density and deposition time. The atomic interaction over wide spatial and temporal scales was depicted by reactive molecular dynamics simulations to assist in understanding the kinetics. Compared to crystalline Li, glassy Li outperforms in electrochemical reversibility, and it has a desired structure for high-energy rechargeable Li batteries. Our findings correlate the crystallinity of the nuclei with the subsequent growth of the nanostructure and morphology, and provide strategies to control and shape the mesostructure of Li metal to achieve high performance in rechargeable Li batteries.

Metal-based anodes, such as those of lithium metal, can lead to the highest specific energy for rechargeable batteries and show great promise to meet the increasing demand for energy storage applications in the future. However, most Li metal electrodes suffer from poor electrochemical reversibility and short cycle life. Since the properties of the Li metal (for example, the nano- and microstructure, morphology and electrochemical performance) in rechargeable Li batteries are largely governed by the electrochemical process, it is critical to comprehend the underlying mechanism of Li deposition by both experimental and theoretical work, especially in the very early stage of nucleation, to seek better control of the Li kinetics.

To explore the electrodeposition behaviour of Li metal, various experimental techniques have been developed to capture the kinetic process and probe the structural evolution of Li metal at different stages and conditions, as displayed in Supplementary Fig. 1 and Supplementary Table 1. Although in situ, operando microscopies allow us to visualize the real-time microstructure evolution[1–7], it is still very difficult to capture the initial stage of Li deposition when Li metal begins to nucleate and subsequently grow into stable microstructures. In order to push the detection limit to the nano or even atomic scale, cryogenic protection is essential to minimize the beam damage, while preserving the intrinsic structure of Li deposits. Recently, cryogenic transmission electron microscopy (cryo-TEM) has proved useful to study the nanostructures of Li metal and reveal the variations in its crystallinity and the solid electrolyte interphases[8,9]. Such variations may substantially alter the growth of Li deposits and their physicochemical properties, yet a detailed understanding has not yet been established.

Classical nucleation theory (CNT) shows that nuclei appear if the embryo's bulk energy overcomes the surface energy, and the nuclei grow if the size of the embryo exceeds the critical radius[10]. For electrochemical nucleation, this process is driven by the charge transfer and sustained by the mass transport of ions near the electrolyte–electrode interface[11]. Previous models based on these principles[7,12–16] underline some key concepts like free energy, surface tension and overpotential, which are macroscopic properties; but these concepts become ambiguous when a nucleus comprises only a few atoms. These properties also do not describe the atomic interactions, attachment kinetics and detachment kinetics to small clusters with sufficient detail to delineate different nanostructure configurations, which is urgently required to develop microscopic and even atomistic models to understand Li nucleation and growth.

Here, we applied cryo-EM to capture the kinetic progression of the nucleation of Li metal and used reactive molecular dynamics (r-MD) simulations to understand the atomic interaction. A disorder–order phase transition (DOPT) was revealed and explained as a function of current density and deposition time. On this basis, the crystallinity of nuclei was correlated with the subsequent growth of the nanostructure and morphology, which are pertinent to the electrochemical performance of the Li metal electrode.

Cryo-TEM observations

The cryo-TEM results (Fig. 1, Supplementary Fig. 2 (ref. [17]) and Supplementary Figs. 3–9) show the nano- and microstructure evolution of electrochemically deposited Li (EDLi) as a function of deposition time (5–20 min; Supplementary Figs. 3–6) and current density (0.1–2.5 mA cm^{-2}; Supplementary Figs. 7–9). At 0.5 mA cm^{-2}, although the deposition time was as short as 5 min, tubular EDLi formed that was about 200 nm in diameter and >1 μm in length (Supplementary Fig. 4). Interestingly, no lattice fringes (Fig. 1a and Supplementary Fig. 5a–d) nor characteristic bright diffraction spots/rings of the body-centred cubic (bcc) Li metal packing in the fast Fourier transformed (FFT) image (Fig. 1d)

[1]Department of NanoEngineering, University of California San Diego, La Jolla, CA, USA. [2]Department of Material Science and Engineering, Idaho National Laboratory, Idaho Falls, ID, USA. [3]Energy and Environmental Directorate, Pacific Northwest National Laboratory, Richland, WA, USA. [4]Department of Energy Storage and Advanced Transportation, Idaho National Laboratory, Idaho Falls, ID, USA. [5]These authors contributed equally: Xuefeng Wang, Gorakh Pawar. ✉e-mail: shirleymeng@ucsd.edu; boryann.liaw@inl.gov

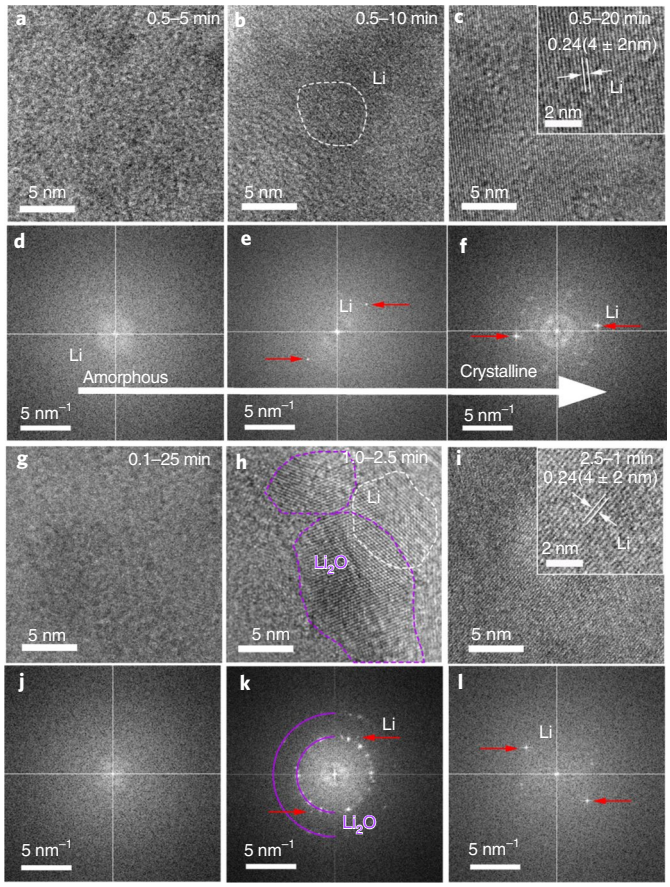

Fig. 1 | Nanostructure evolution of Li deposit as a function of deposition time and current density. a–l, Cryo-TEM images (**a–c** and **g–i**) and their corresponding FFT patterns (**d–f** and **j–l**) of the Li deposits at 0.5 mA cm^{-2} for 5 min (**a** and **d**), 10 min (**b** and **e**) and 20 min (**c** and **f**); 0.1 mA cm^{-2} for 25 min (**g** and **j**); 1.0 mA cm^{-2} for 2.5 min (**h** and **k**); and 2.5 mA cm^{-2} for 1.0 min (**i** and **l**). The images with the Li metal lattice and the characteristic bright diffraction spots highlighted by the red arrows are from the (110) plane of Li metal.

were found, suggesting that the EDLi is amorphous or glassy. The local structure in Fig. 1a displays the disordered arrangement of Li atoms (comparison to those in Fig. 1c and Supplementary Fig. 6). At 10 min, a small portion of EDLi near the surface became crystalline (Fig. 1b and Supplementary Fig. 5e–h), as evidenced by the characteristic bright diffraction spots (highlighted by the red arrows) in Fig. 1e with weak contrast. Lattice fringes were present in this region (Fig. 1b), and the distance between the adjacent fringes was measured to be 0.24(4 ± 2) nm, consistent with the spacing between Li (110) planes[18]. The domain of the crystalline EDLi (shown by the white dashed line) is about 5 ± 3 nm in size, a size for which the r-MD simulation predicted the transition to the crystalline phase would be eminent and spontaneous. The crystallinity degree of the EDLi is further enhanced with increased deposition time. For 20 min, large crystalline domains (>50 nm) and intense characteristic bright diffraction spots of the bcc structure were present (Fig. 1c,f, Supplementary Fig. 5i–l and Supplementary Fig. 6). Thus, at the same deposition rate, as the deposition time increases, more Li atoms aggregate to form larger clusters. Once the cluster is larger than a critical size, the DOPT occurs.

Further studies of the nanostructure dependence on current density (Fig. 1g–l for constant capacity and Supplementary Fig. 7) showed that the higher the current density used, the larger the cluster size and the higher the degree of crystallinity in EDLi (the statistical analysis is shown in Supplementary Fig. 8). The EDLi is mostly amorphous at 0.1 mA cm^{-2} (Fig. 1g,j and Supplementary Fig. 7a,e,i,m), partly crystalline at 1.0 mA cm^{-2} (Fig. 1h,k and Supplementary Fig. 7c,g,k,o) and highly crystalline at 2.5 mA cm^{-2} (Fig. 1i,l and Supplementary Fig. 7d,h,l,p). The crystalline domains of EDLi at 1.0 mA cm^{-2} were found near the surface (labelled by the red square in Supplementary Fig. 7c) and about 5 ± 3 nm in size (labelled by the white dashed line in Fig. 1h). These results suggest that (1) the cluster size is key to the DOPT, (2) matured crystallites are often larger than 5 nm and (3) the crystalline cluster size is sensitive to the current density. Thus, high current densities expedite the Li aggregation to precipitate the crystalline nuclei. This result implies that a diverse local current density may lead to a wider distribution of Li cluster sizes with varied morphology (Supplementary Fig. 9).

Obtaining glassy EDLi during electrodeposition is quite surprising for alkali metals but not preposterous, since DOPT was also observed in other metals (such as Ni, Au, Ag, Pt_3Co, FePt and so on) during nucleation and growth in solid or solution with precursors via in situ annealing and by liquid-cell electron microscopy[19–23]. These DOPTs deviate from the single-step process explained by the CNT and suggest the multi-step nature of crystallization through amorphous interphases. All the DOPT critical sizes are around 5–8 nm.

The r-MD simulations

To understand the peculiar glassy nature of the EDLi, a three-stage r-MD protocol was used to simulate the nucleation process with a variety of discrete canonical ensembles and conditions typically comprising (1) heating at 500 K for 0.1 ns to provide sufficient driving force for the nucleation, (2) quenching to 300 K with a cooling rate of 1 K ps^{-1} and (3) equilibrating at 300 K for 5 ns (Fig. 2a). The reactive force field ReaxFF potential[24] was used to simulate the Li–Li interactions and the Large-scale Atomic/Molecular Massively Parallel Simulator (LAMMPS) package[25,26] to perform all simulations (Extended Data Fig. 1 and Supplementary Figs. 10–13)[27–31]. In the heating and quenching stage, the nucleation sites dynamically evolved into more stable clusters, as Ostwald ripening explains (Fig. 2a)[32]. Such a condensation process requires a specific 'incubation time' to give the birth of a stable crystalline cluster, which has been overlooked by the quasi-equilibrium models including the CNT or density function theory to date. Intriguingly, all clusters studied here were disordered at the end of quenching, far away from the stable, ordered crystalline state. Thus, the incubation and condensation process is key to dictating the time to reach a stable lattice structure, depending on the ensemble size and the initial energy state given (Fig. 2b–d and Supplementary Fig. 10).

Figure 2b illustrates a sampling of the lattice structure of Li clusters as a function of cluster size at the end of the simulation. Lithium clusters with >700 Li atoms in the ensemble (at a packing density of $\rho = 0.0534\,g\,cm^{-3}$) are able to transform into a nucleus with the bcc lattice structure, whereas those with <700 Li atoms remain disordered or glassy. Clusters of 700 Li atoms exhibit either a glassy or crystalline state with a broad range of kinetic pathways and incubation times (Fig. 2c). Thus, a cluster of 700 Li atoms, with a size of about 2–3 nm, sets the threshold for the DOPT. Increasing the current density yields a larger cluster size, which rapidly reduces the incubation time for the DOPT (Fig. 2c) and increases the fraction of bcc ordered or crystalline Li in the lattice (Fig. 2d). If the current density is lower than the threshold, the incubation time for the DOPT is on the order of nanoseconds, which is rarely emphasized by the CNT[33,34].

As Li aggregates, the incubation and physical spatial confinement from the neighbouring bodies determine if a cluster has sufficient exergy (primarily entropy), mobility and time to carry out

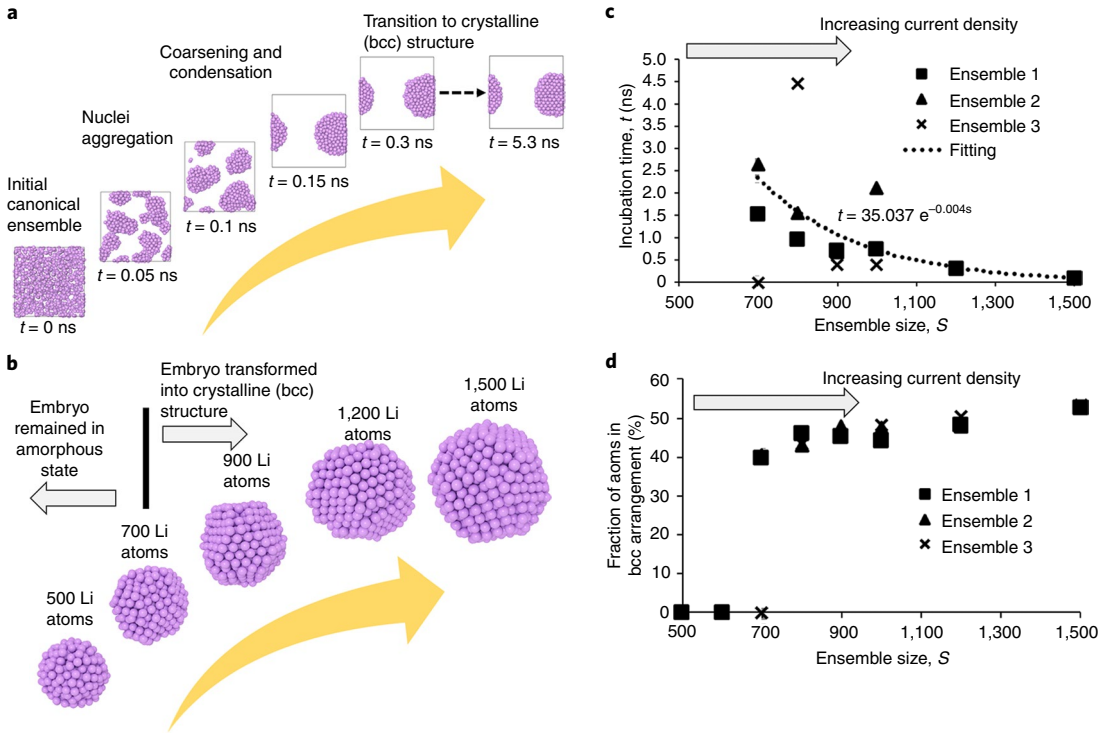

Fig. 2 | MD simulation of the nucleation process of Li metal. a, An example of Li nucleation, growth and kinetic pathway to a cluster with an ensemble of 700 Li atoms. **b**, A sampling of the final state of various sizes of clusters at the end of the simulation (5.3 ns). **c**, Incubation time to DOPT (a second-order phase transition) as a function of ensemble size. **d**, Fraction of Li atoms in a bcc lattice arrangement as a function of ensemble size.

the DOPT. Extended Data Fig. 1 illustrates the variability in the kinetic pathways and temporal nanostructure evolutions in terms of packing density, mass and energy exchange. At a low packing density of 0.0534 g cm^{-3} (Extended Data Fig. 1a), whether mass or energy exchange was confined or not, the Li aggregation produces mostly glassy phases. As the current density increases, the packing density of Li atoms increases in proportion (Extended Data Fig. 1b–d). Further confinement in mass and energy exchange expedite the DOPT and shorten the incubation time. Diverse kinetic results determine the microstructure and morphological evolutions: from spherical glassy nanostructures of a random distribution of sizes to a host of microstructures of diverse crystallinity, including sheets and rods that comprise glassy nanostructures (Extended Data Fig. 1a and glassy part of Extended Data Fig. 1b), mixtures of crystalline nanostructures of various sizes and shapes (crystalline part of Extended Data Fig. 1b,c) and connected networks of micro-grains and micro-pores (Extended Data Fig. 1d). Such a dynamic range of atomic lattice arrangements further affects the subsequent larger-size microstructure evolutions, crystallinity and morphological and shape changes in a solid particle. A larger scale (in the linear dimension of 20 nm) of simulation and representation of this behaviour is shown in Supplementary Fig. 13.

From nucleation to growth

The microstructure and morphology of the Li deposited to a 1 mA h cm^{-2} loading were examined by scanning electron microscopy (SEM) and cryo-TEM (Fig. 3, Extended Data Figs. 2 and 3 and Supplementary Figs. 14–17). The results in Fig. 3 are consistent with the simulation prediction. Most of the Li metals grown at 0.1 mA cm^{-2} have a sheet-like morphology, and their planar size can be as large as several micrometres (Fig. 3a,d,g). This large sheet originates from the glassy nature of the Li nuclei, which mostly remained at the end of the growth (Fig. 3j). By contrast, the Li metals grown at

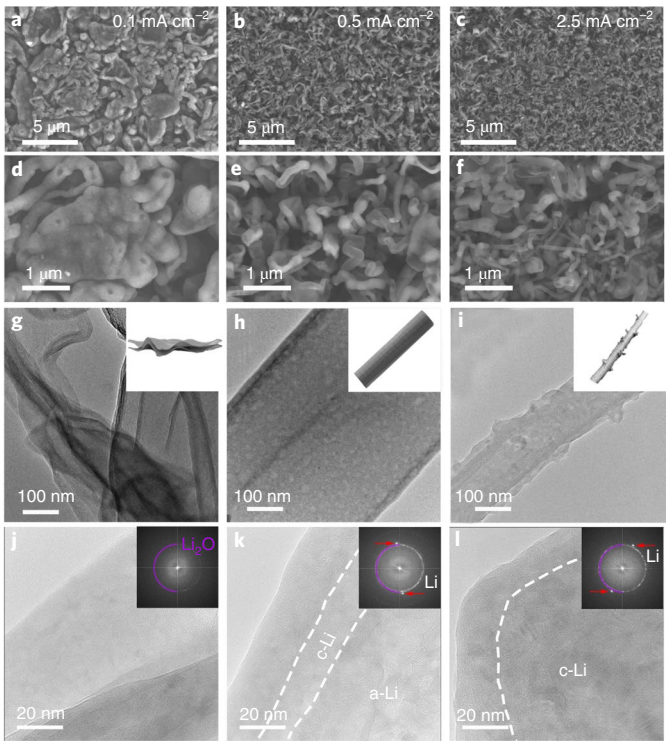

Fig. 3 | Microstructure and morphology of Li deposits after 1 mA h cm^{-2} plating. a–l, SEM (**a–f**) and cryo-TEM images (**g–l**) of the Li deposits at 0.1 mA cm^{-2} for 10 h (**a**,**d**,**g**,**j**), 0.5 mA cm^{-2} for 2 h (**b**,**e**,**h**,**k**) and 2.5 mA cm^{-2} for 0.4 h (**c**,**f**,**i**,**l**). The images with the Li metal lattice and the characteristic bright diffraction spots highlighted by the red arrows are from the (110) plane of Li metal.

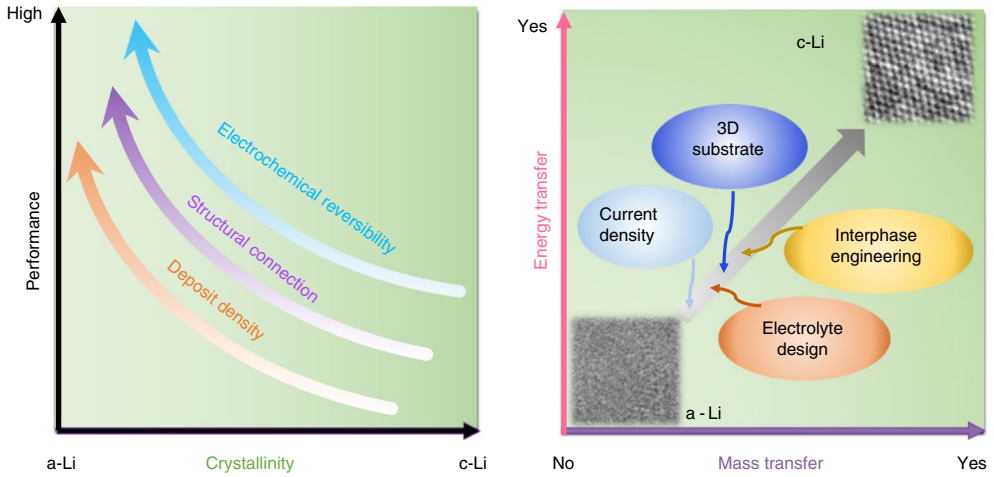

Fig. 4 | Correlation between crystallinity of Li metal and performance (left) and strategies to achieve better performance (right). The performance (left) is specified as the electrochemical performance of Li metal as an anode for Li metal batteries, including high Coulombic efficiency (CE), long cycling life, low volume change and absence of Li dendrites. The structural connection is referred to as the capability to maintain the electronic and ionic pathway for charge transfer and ion transportation; poor structural connection will facilitate lost electrochemical activity and form 'dead' Li. The electrochemical reversibility is measured by the content ratio of the stripped Li by plated Li, which should be close to 100%. The ideal deposit density should be consistent with the theoretical density of Li metal (0.534 g cm^{-3}). The proposed strategies such as using the 3D substrate, changing current density, engineering interphase and designing electrolytes can alter the energy transfer and mass transfer of EDLi during nucleation and growth, thus resulting in varied crystallinity of EDLi.

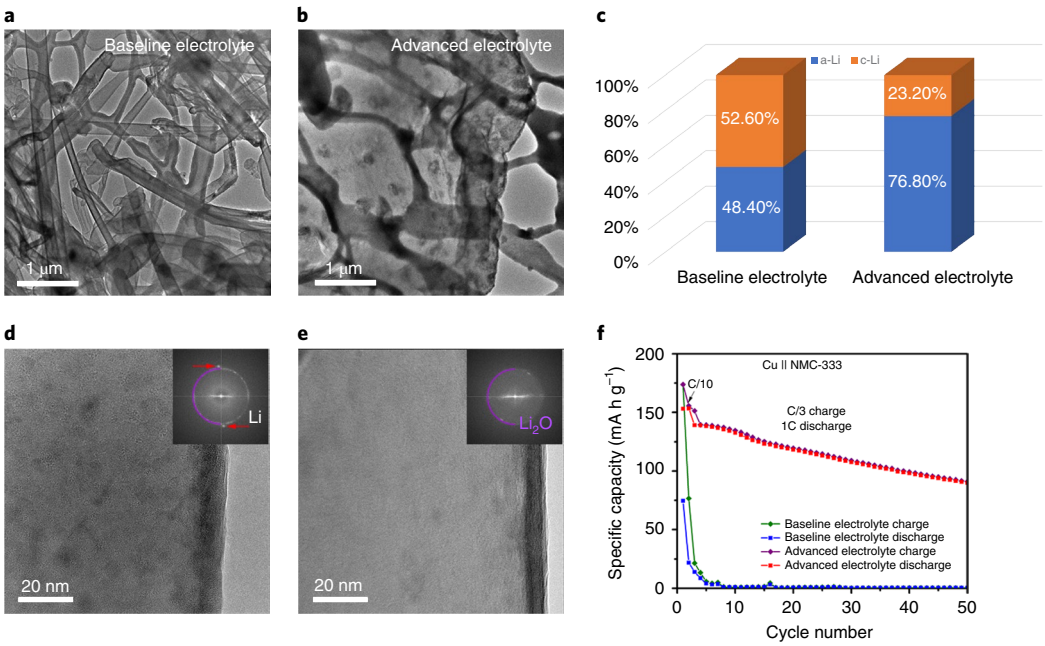

Fig. 5 | The influence of electrolyte on the nano- and microstructure of Li deposits and the resulting performance. a–e, Nanostructure (**d** and **e**) and microstructure (**a** and **b**) of Li deposits from baseline electrolyte (**a** and **d**) and advanced electrolyte (**b** and **e**); statistical distribution (**c**) of a-Li and c-Li in the two electrolytes. **f**, A comparison of the cycling performance of two electrolytes using Li-free anode Cu || NMC-333 cells. The images with the Li metal lattice and the characteristic bright diffraction spots highlighted by the red arrows are from the (110) plane of Li metal. The statistical analysis was performed based on the ~100 separated random Li ribbons; c-Li was counted if the present lattice or FFT diffraction spots belonged to Li metal; otherwise, a-Li was counted. 1C was equal to a current density of 1.5 mA cm^{-2}.

0.5 and 2.5 mA cm^{-2} are partially (Fig. 3k) and highly (Fig. 3l) crystalline (Supplementary Figs. 14–17). As a result, ribbon- and even dendrite-like Li deposits are formed at 0.5 mA cm^{-2} (Fig. 3b,e,h) and 2.5 mA cm^{-2} (Fig. 3c,f,i), with a rapidly reduced planar diameter and lower Coulombic efficiency (Supplementary Fig. 16). Thus, it is reasonable to correlate the microstructure, morphology and performance of Li deposits with the order–disorder nanostructure of the Li nuclei: the higher the crystallinity, the finer the final shape and the lower the electrochemical reversibility. The initial nucleation shapes the subsequent growth of the Li metal deposits.

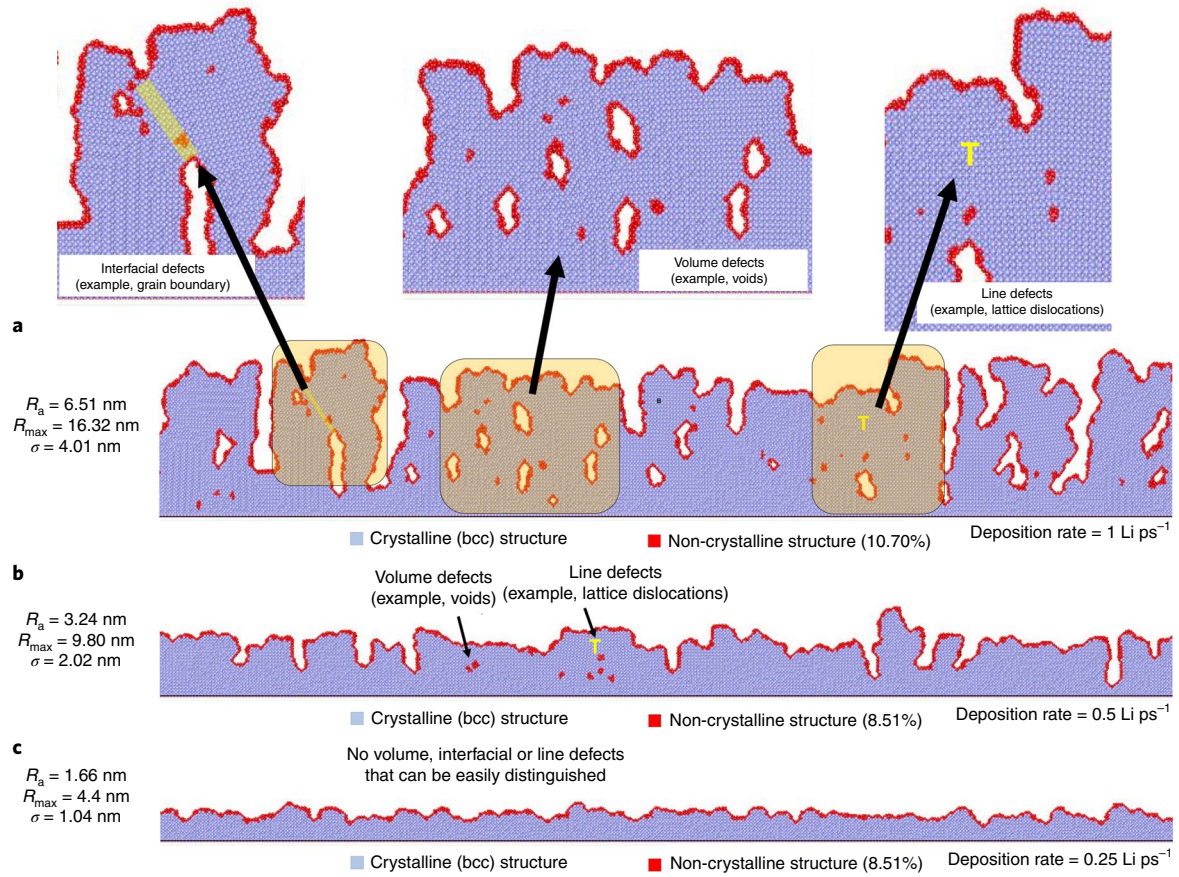

Fig. 6 | Simulated results of Li deposition at three different rates. a, 1 Li ps^{-1}. **b**, 0.5 Li ps^{-1}. **c**, 0.25 Li ps^{-1}. A quasi-3D simulation domain of 112.3 (*L*) × 0.702 (*D*) × 35.1 (*H*) nm^3 was used to simulate the rate effects on the Li deposit. *L*, length; *D*, depth; *H*, height. The modified embedded atom model (MEAM) force field was used to capture the Li atomic interactions. The LAMMPS simulation package was used to perform all atomistic simulations where the total simulation time was 45 ns with a time step of 1 fs. The quality and characteristics of the Li deposition are quantified by three parameters: an average surface roughness (R_a), the maximum surface roughness (R_{max}) and the standard deviation of surface roughness (σ).

Strategies and applications

Figure 4 illustrates the benefits of glassy Li metal as a rechargeable Li battery anode. The glassy nature (that is, the absence of the ordered nanostructure, grain boundaries and crystal defects) of the Li metal avoids epitaxial growth and enables multi-dimensional growth into large grains, which is the desired form for a practical Li metal anode. The Li grains have higher density, lower porosity and tortuosity, less reactivity and better microstructure interconnections than the dendrites. These features can substantially minimize the volume expansion, reduce the side reaction between Li and the electrolyte and maintain an effective electronic and ionic network or percolation pathway. As a consequence, a higher electrochemical reversibility would be expected for glassy Li. Therefore, from a structural perspective, glassy Li metal may be the key to solve the long-standing cyclability issue of using a Li metal electrode for high-energy rechargeable Li batteries.

As demonstrated above, the DOPT is regulated by the packing density, energy transfer and mass transfer during the nucleation process, which in turn provide the ways to facilitate the formation of favourable glassy Li metal. Reducing the current density down to the critical point will directly decrease the initial packing density and facilitate a longer incubation. An alternative way is to use the three-dimensional (3D) substrate (current collector) to reduce the effective local current density. Meanwhile, fast ion and electron conduction is advantageous to reduce mass transfer and energy transfer barriers during the nucleation and growth process, which requires electrolyte design and interphase engineering. These strategies have been proved effective to obtain larger grains of Li with enhanced reversibility, although prior studies have not been able to correlate the intrinsic nature of amorphous or glassy Li with the improved performance. Herein, we provide a microscopic perspective on the working principle of these strategies and propose that they could actually alter the nano- and microstructure of Li deposits.

As a proof of concept, Fig. 5 shows that the electrolyte design does indeed dramatically influence the bulk lattice structure (Fig. 5c–e) of the Li deposits, which regulates the final morphology (Fig. 5a,b) and electrochemical performance (Fig. 5f). Statistical analysis results (Fig. 5c) indicate that the advanced electrolyte is in favour of forming amorphous Li (a-Li) deposits (~76.8% a-Li versus 23.2% crystalline Li (c-Li)), while the crystalline ones are dominant in the baseline electrolyte (~48.4% a-Li versus 52.6% c-Li). For their nanostructure, the lattice structure is predominantly disordered in the former (Fig. 5e), but a mixture of ordered and disordered segments appear in the latter (Fig. 5d); whereas both display similar surface solid–electrolyte interphase structure (~10 nm thick and composed of Li_2O nanocrystals; black regime). This result demonstrates that it is the intrinsic nanostructure property of Li that governed the final shape and performance of the Li metal anode. As a result, long and thin ribbon-like Li deposits (Fig. 5a) were formed in the baseline electrolyte while large chunky deposits of Li were found in the advanced electrolyte (Fig. 5b). In Li-free Cu||NMC-333 cells (NMC-333, one-third nickel, one-third manganese and

one-third cobalt; Fig. 5f), the cell with baseline electrolyte failed quickly within five cycles, while the advanced electrolyte-based cell lasted for more than 50 cycles with a capacity retention of 59.2% (Supplementary Table 2). This result further proves that the glassy Li metal is beneficial to achieve the best electrochemical performance for high-energy rechargeable Li batteries.

A combination of the cryogenic microscopic observations and molecular-level simulations presents an explicit picture of the intermediate structural and morphological evolution of Li deposits from the atomic scale to a microscale particle. Depending on the atomic interaction during the initial nucleation (for example, the atoms' packing density, mass transfer and energy transfer), the nanostructure of Li nuclei can vary from disordered to ordered, which eventually shapes the final microstructure and affects the performance. To further illustrate this aspect, Fig. 6 provides an interesting simulation on how the deposition rate affects the morphology evolution and kinetic variation in shaping the surface landscape and defect formation in the bulk. At a higher rate (Fig. 6a), less incubation time could afford a more stabilized growth of c-Li in the EDLi to create larger grains in the microstructure. However, the mismatch of the orientation among the grains could result in a rougher surface and a substantial amount of defect formation from dislocations and grain boundaries to voids. As the Li deposition rate decreases, a smoother surface and less defects in the bulk developed in the microstructure and morphology.

For rechargeable Li batteries, glassy Li has been proven to possess the desired nanostructure since it facilitates the formation of large Li grains and achieves high Coulombic efficiency. The absence of the ordered nanostructure and grain boundaries enables Li metal to grow in multiple dimensions rather than in an epitaxial manner, and to maintain good structural connection and reversibility during plating and stripping. Tuning the temporal and spatial confinements in mass transfer and energy transfer by different strategies could help to obtain glassy Li metal deposits, including methods to lower the current density, design advanced electrolyte compositions and use 3D current collectors. These strategies are able to alter the bulk microstructure of a Li metal electrode and obtain larger, more homogeneous Li deposits with improved cycling performance.

Amorphous metals or metallic glasses are attractive as a class of advanced functional materials for applications in different technological areas, and scientific exploration of glass formation and glassy phenomena need more attention[35–38]. Conventional metallic glasses are made by alloying more than two metals, especially transition metals, by fast quenching (for example, $>10^6\,K\,s^{-1}$)[35]. This work demonstrates that electrochemical deposition is a powerful and effective method to obtain such metallic glasses, including Na, K, Mg and Zn (Extended Data Fig. 4 and Supplementary Figs. 18–21). More importantly, the properties of such metallic glasses, the amounts and the particle sizes and distributions could be tuned by adjusting the current density and deposition time through optimization. These new amorphous active metals will open new opportunities in various applications besides the metallic glass and energy storage fields, including biomedicine, nanotechnology and microelectromechanical systems.

Online content

Any methods, additional references, Nature Research reporting summaries, source data, extended data, supplementary information, acknowledgements, peer review information; details of author contributions and competing interests; and statements of data and code availability are available at https://doi.org/10.1038/s41563-020-0729-1.

Received: 31 October 2019; Accepted: 9 June 2020;
Published online: 27 July 2020

References

1. Steiger, J., Kramer, D. & Mönig, R. Mechanisms of dendritic growth investigated by in situ light microscopy during electrodeposition and dissolution of lithium. *J. Power Sources* **261**, 112–119 (2014).
2. Wood, K. N. et al. Dendrites and pits: untangling the complex behavior of lithium metal anodes through operando video microscopy. *ACS Cent. Sci.* **2**, 790–801 (2016).
3. Cohen, Y. S., Cohen, Y. & Aurbach, D. Micromorphological studies of lithium electrodes in alkyl carbonate solutions using in situ atomic force microscopy. *J. Phys. Chem. B* **104**, 12282–12291 (2000).
4. Mogi, R., Inaba, M., Iriyama, Y., Abe, T. & Ogumi, Z. In situ atomic force microscopy study on lithium deposition on nickel substrates at elevated temperatures. *J. Electrochem. Soc.* **149**, A385–A390 (2002).
5. Orsini, F. et al. In situ scanning electron microscopy (SEM) observation of interfaces within plastic lithium batteries. *J. Power Sources* **76**, 19–29 (1998).
6. Cheng, J.-H. et al. Visualization of lithium plating and stripping via in operando transmission X-ray microscopy. *J. Phys. Chem. C* **121**, 7761–7766 (2017).
7. Kushima, A. et al. Liquid cell transmission electron microscopy observation of lithium metal growth and dissolution: root growth, dead lithium and lithium flotsams. *Nano Energy* **32**, 271–279 (2017).
8. Li, Y. et al. Atomic structure of sensitive battery materials and interfaces revealed by cryo–electron microscopy. *Science* **358**, 506–510 (2017).
9. Wang, X. et al. New insights on the structure of electrochemically deposited lithium metal and its solid electrolyte interphases via cryogenic TEM. *Nano Lett.* **17**, 7606–7612 (2017).
10. Dubrovskii, V. in *Nucleation Theory and Growth of Nanostructures* 1–73 (Springer, 2014).
11. Scharifker, B. R. & Mostany, J. in *Encyclopedia of Electrochemistry* 512–539 (Wiley, 2007).
12. Ely, D. R., Jana, A. & García, R. E. Phase field kinetics of lithium electrodeposits. *J. Power Sources* **272**, 581–594 (2014).
13. Ely, D. R. & García, R. E. Heterogeneous nucleation and growth of lithium electrodeposits on negative electrodes. *J. Electrochem. Soc.* **160**, A662–A668 (2013).
14. Akolkar, R. Modeling dendrite growth during lithium electrodeposition at sub-ambient temperature. *J. Power Sources* **246**, 84–89 (2014).
15. Akolkar, R. Mathematical model of the dendritic growth during lithium electrodeposition. *J. Power Sources* **232**, 23–28 (2013).
16. Chazalviel, J. N. Electrochemical aspects of the generation of ramified metallic electrodeposits. *Phys. Rev. A* **42**, 7355–7367 (1990).
17. Wang, X., Li, Y. & Meng, Y. S. Cryogenic electron microscopy for characterizing and diagnosing batteries. *Joule* **2**, 2225–2234 (2018).
18. Wang, F. et al. Chemical distribution and bonding of lithium in intercalated graphite: identification with optimized electron energy loss spectroscopy. *ACS Nano* **5**, 1190–1197 (2011).
19. Loh, N. D. et al. Multistep nucleation of nanocrystals in aqueous solution. *Nat. Chem.* **9**, 77–82 (2017).
20. Yang, J. et al. Amorphous-phase-mediated crystallization of Ni nanocrystals revealed by high-resolution liquid-phase electron microscopy. *J. Am. Chem. Soc.* **141**, 763–768 (2019).
21. Liao, H.-G., Cui, L., Whitelam, S. & Zheng, H. Real-time imaging of Pt_3Fe nanorod growth in solution. *Science* **336**, 1011–1014 (2012).
22. Wittig, J. E., Bentley, J. & Allard, L. F. In situ investigation of ordering phase transformations in FePt magnetic nanoparticles. *Ultramicroscopy* **176**, 218–232 (2017).
23. Chi, M. et al. Surface faceting and elemental diffusion behaviour at atomic scale for alloy nanoparticles during in situ annealing. *Nat. Commun.* **6**, 8925 (2015).
24. van Duin, A. C. T., Dasgupta, S., Lorant, F. & Goddard, W. A. ReaxFF: a reactive force field for hydrocarbons. *J. Phys. Chem. A* **105**, 9396–9409 (2001).
25. Plimpton, S., Crozier, P. & Thompson, A. LAMMPS-large-scale atomic/molecular massively parallel simulator. *Sandia Natl Laboratories* **18**, 43 (2007).
26. Majure, D. L. et al. Large-scale atomic/molecular massively parallel simulator (LAMMPS) simulations of the effects of chirality and diameter on the pullout force in a carbon nanotube bundle. In *2008 DoD HPCMP Users Group Conference* 201–207 (IEEE, 2008).
27. Stukowski, A. Visualization and analysis of atomistic simulation data with OVITO–the open visualization tool. *Model. Simul. Mater. Sci. Eng.* **18**, 015012 (2009).
28. Onofrio, N. & Strachan, A. Voltage equilibration for reactive atomistic simulations of electrochemical processes. *J. Chem. Phys.* **143**, 054109 (2015).
29. Jensen, B. D., Wise, K. E. & Odegard, G. M. The effect of time step, thermostat, and strain rate on ReaxFF simulations of mechanical failure in diamond, graphene, and carbon nanotube. *J. Comput. Chem.* **36**, 1587–1596 (2015).

30. Cui, Z., Gao, F., Cui, Z. & Qu, J. Developing a second nearest-neighbor modified embedded atom method interatomic potential for lithium. *Model. Simul. Mater. Sci. Eng.* **20**, 015014 (2011).
31. Stukowski, A. Structure identification methods for atomistic simulations of crystalline materials. *Model. Simul. Mater. Sci. Eng.* **20**, 045021 (2012).
32. Baldan, A. Review progress in Ostwald ripening theories and their applications to nickel-base superalloys part I: Ostwald ripening theories. *J. Mater. Sci.* **37**, 2171–2202 (2002).
33. Nanev, C. N. in *Handbook of Crystal Growth* 2nd edn, 315–358 (Elsevier, 2015).
34. Karthika, S., Radhakrishnan, T. K. & Kalaichelvi, P. A review of classical and nonclassical nucleation theories. *Cryst. Growth Des.* **16**, 6663–6681 (2016).
35. Greer, A. L. Metallic glasses. *Science* **267**, 1947–1953 (1995).
36. Jafary-Zadeh, M. et al. A critical review on metallic glasses as structural materials for cardiovascular stent applications. *J. Funct. Biomater.* **9**, 19 (2018).
37. Chen, M. A brief overview of bulk metallic glasses. *NPG Asia Mater.* **3**, 82–90 (2011).
38. Khan, M. M. et al. Recent advancements in bulk metallic glasses and their applications: a review. *Crit. Rev. Solid State Mater. Sci.* **43**, 233–268 (2018).

Methods

EDLi. The electrolyte for Li metal deposition was commercial LP50 (BASF), which consists of 1.0 mol l^{-1} (1.0 M) lithium hexafluorophosphate ($LiPF_6$) in ethylene carbonate/ethyl methyl carbonate (EC/EMC, 50/50 wt%). The advanced electrolyte was a localized high-concentration electrolyte composed of lithium bis(fluorosulfonyl)imide (LiFSI), 1,2-dimethoxyethane (DME) and 1,1,2,2-tetrafluoroethyl-2,2,3,3-tetrafluoropropyl ether (TTE) at a molar ratio of 1:1.2:3. Na metal was deposited from the electrolyte containing 1.0 M sodium hexafluorophosphate ($NaPF_6$) in propylene carbonate (PC). The electrolyte for K plating was 1.0 M potassium hexafluorophosphate (KPF_6) in DME. A combination of phenyl magnesium chloride (PhMgCl) and aluminium chloride ($AlCl_3$) in tetrahydrofuran (THF) was used for the Mg deposition, and its concentration was 0.25 M. The Zn metal was obtained from the electrolyte of 0.25 M zinc bis(trifluoromethanesulfonyl) imide ($Zn(TFSI)_2$) in DME. These materials were stored and handled in a glovebox with <0.1 ppm H_2O and <0.1 ppm O_2.

The samples for the cryo-TEM were prepared by electrochemical deposition of metal species directly onto a lacey carbon grid in a coin cell. After deposition, the grid was harvested from the cell and lightly rinsed with dimethyl carbonate (DMC) or DME to remove any trace amount of salt on the grid in the glovebox. For the Li metal samples, both types of sample transfer methods were used in this work; the data shows identical trends and leads to the same conclusions. A cooling holder was used for the Mg and Zn metals while a cryo-transfer holder was used for the Na and K. When the cooling holder was used, the TEM samples were loaded on the holders in the homemade glovebox purged with continuous Ar gas at a pressure of 50 ml min^{-1}. Then the cooling holder with samples was transferred to the TEM at room temperature while the same Ar purging was continuously followed with the samples. Liquid N_2 was added in the cooling holder; it took about 1 h for samples to reach and stabilize at the temperature around 100 K. When the cryo-transfer holder was used, the samples were taken out from the well-sealed container and quickly immersed into the liquid N_2 in the homemade glovebox purged with continuous Ar gas at a pressure of 50 ml min^{-1}. The cryo-transfer holder was cooled first, and then the sample was loaded onto it in the liquid N_2. The cryo-transfer holder with samples was transferred to the TEM at the cryo temperature. The cryo-TEM micrographs were recorded on a JEM-2100F cryo-TEM equipped with OneView and K2 cameras and a field-emission gun operated at 200 keV. The images were taken at a magnification of ×500,000 with a dose of ~70 e $Å^{-2}$ s^{-1} when the temperature of the samples reached about 100 K. All the sample preparation processes avoided any exposure to air to minimize possible chemical alterations to the samples. Detailed sample preparation and transfer procedures have been reported in a previous reference[17] and are summarized in Supplementary Fig. 2. Electron energy loss spectroscopy (EELS) was performed on the JEOL Grand Arm 300CF TEM/STEM operated at 300 kV. The spectra of the Li K edge were acquired from an energy of 20–90 eV with a pixel size of 1 eV and exposure time of 1.0 s, and processed with a subtracted background. The energy resolution of EELS is 0.7 eV. SEM images were recorded with Zeiss Sigma 500 field-emission scanning electron microscopy on a JEOL JSM-6700F operating at 10 kV. The X-ray diffraction signals were collected on an X'Pert Pro MPD X-ray diffractometer (D8 Advance with a LynxEye_XEdetector, Bruker) with Cu KR1 radiation ($\lambda = 1.5405$ Å), and Kapton tape was used to seal the Li deposits.

The r-MD computation details. The r-MD simulation technique was used to simulate the complex atomic-scale Li nucleation, coarsening, condensation and phase transition in the kinetic pathway towards phase stability, over a temporal scale of a few nanoseconds. In this process, we retain the causality and accuracy of the quantum mechanical calculations while minimizing the computational burden. A general ReaxFF reactive force field[24] dependent on bond order and bond distance was used to model all atomic interactions. The ReaxFF reactive force field enabled the dynamic formation and breaking of the Li–Li chemical bonds during simulation. Various bond-order-dependent and bond-order-independent energy terms contributed to the total ReaxFF force field energy, where the total energy is given by the following:

$$E_{\text{total}} = E_{\text{b}} + E_{\text{over}} + E_{\text{under}} + E_{\text{lp}} + E_{\text{val}} + E_{\text{tor}} + E_{\text{vdw}} + E_{\text{Coul}} \quad (1)$$

where E_{b}, E_{over}, E_{under}, E_{lp}, E_{val}, E_{tor}, E_{vdw} and E_{Coul} are the bond, over-coordination, under-coordination, lone-pair, valence, torsion, van der Waals and Coulombic contributions, respectively. A detailed description of the partial energy contributions and their bond-order dependence and/or independence can be found in the literature[24]. The accuracy and the transferability of the ReaxFF reactive force field are typically dictated by the quality of the quantum mechanical data (or the training set) used during the ReaxFF force field parameterization. The Li ReaxFF force field parameters used in this investigation were extensively trained to reproduce the phase stability, the equation of the state, the lattice parameters and the cohesive energies of different Li metal phases.

Various possible atomistic configurations were investigated by varying the system size (that is, ensembles with the total number of Li atoms in the system in the range of 500–1,500 atoms) and the initial energy state of each configuration (the 3D position of Li atoms) on the potential energy surface. Each ensemble could be equated to a unique situation in current density. A systematic heating, quenching and equilibration protocol was used to perform all energy minimization simulations, aiming to capture the temporal evolution of Li atom aggregation during their nucleation, coarsening and condensation stages towards phase stability. The simulated protocol included heating of the Li atoms confined in a canonical (NVT) ensemble ($\rho = 0.0534$ g cm^{-3}) at 500 K for 0.1 ns, quenching to 300 K for 0.2 ns and equilibration for 5 ns to allow energy minimization at 300 K. The time integration of the Nose–Hoover-style non-Hamiltonian equations of motion was used to generate atom positions and velocities sampled from the NVT ensemble. A time step of 0.5 fs was used in all simulations unless specified.

The influence of the additional constraints including the energy transfer (for example, systems with and without heating and quenching before equilibration), the mass transfer (for example, systems with periodic and non-periodic boundary conditions) and the confinement level (for example, systems with a packing density of $\rho = 0.13$, 0.26 and 0.47 g cm^{-3}) were also investigated with ensembles comprised of 600 Li atoms in a case study. Furthermore, additional simulations were performed with ensembles of 600 Li atoms ($\rho = 0.0534$ g cm^{-3}) with relatively shorter time steps (0.1 fs and 0.25 fs) to investigate the sensitivity of the causality dependence on the time step. All initial molecular configurations were generated and the simulation set-up performed in the Scienomics MAPS interface environment (Version 4.0.1, 2016), whereas LAMMPS molecular dynamics simulation code was used to perform all atomistic simulations[25]. Finally, all visualizations of the atomic trajectory were performed with the Ovito program[27].

To determine and estimate the fraction of Li atoms in the ensemble that constitute the bcc lattice structure (that is, to distinguish different phases and estimate their relative abundance), the adaptive common neighbour analysis (a-CNA) method proposed by Stukowski et al.[27,31] was used. The a-CNA method uses the local cut-off distance (determined from the nearest neighbouring atoms) as the criterion to identify and distinguish a typical phase (for example bcc, fcc or hcp stacking in the lattice) in a given lattice structure.

A quasi-3D aerial surface area of 112.3 (L) × 0.702 (D) × 35.1 (H) nm^3 was used here to simulate the rate effects on Li deposition. Three Li deposition rates, 1 Li ps^{-1} (high), 0.5 Li ps^{-1} (medium) and 0.25 Li ps^{-1} (low), were used. The total simulation time was 45 ns with a time step of 1 fs in each case. All simulations were performed with the LAMMPS simulation package and MEAM force field.

Data availability

The data that support the findings of this study are available from the corresponding authors upon reasonable request. Source data are provided with this paper.

Acknowledgements

We thank the UC Irvine Materials Research Institute (IMRI) for the use of the Cryo-Electron Microscopy Facility and Kratos XPS, funded in part by the National Science Foundation Major Research Instrumentation Program under grant no. CHE-1338173. We thank X. Pan, T. Aoki, L. Xing and J.-G. Zheng for their assistance with the microscopy. Work at the Molecular Foundry was supported by the Office of Science, Office of Basic Energy Sciences, of the US Department of Energy under contract no. DE-AC02-05CH11231. The SEM was performed in part at the San Diego Nanotechnology Infrastructure (SDNI), a member of the National Nanotechnology Coordinated Infrastructure, which is supported by the National Science Foundation (grant ECCS-1542148). We also thank A. van Duin of the Pennsylvania State University for providing the ReaxFF parameters used in this work. We thank W. Xu and M. Olguin for discussing the results. This work is supported by the Assistant Secretary for Energy Efficiency and Renewable Energy, Office of Vehicle Technologies of the US Department of Energy in the Advanced Battery Materials Research (BMR) Program (Battery500 Consortium). Idaho National Laboratory (INL) is operated by Battelle Energy Alliance under contract no. DE-DE-AC07-05ID14517 for the US Department of Energy.

Author contributions

X.W., Y.S.M. and B.L. conceived the idea. X.W. designed the experiments and conducted the cryo-TEM. Y.L., B.L., M.Z. and A.B. helped with cell making, electrochemical performance evaluation, EELS and SEM. X.W., Y.L. and Y.S.M. analysed and discussed the experimental data. X.W. and Y.L. made the schematic images. G.P., E.D. and B.L. developed the concept of the r-MD approach. G.P. conducted the simulation work. B.L. provided the major interpretation and discussion of the r-MD results in the paper. X.R. and J.Z. provided the advanced electrolyte and the anode-free electrochemical performance. P.L., J.X., J.L. and E.D. participated in discussing the results and commenting on the manuscript. The manuscript was mainly written and revised by X.W., B.L., G.P. and Y.S.M. All authors approved the final version of the manuscript.

Competing interests

The authors declare no competing interests.

Additional information

Extended data is available for this paper at https://doi.org/10.1038/s41563-020-0729-1.

Supplementary information is available for this paper at https://doi.org/10.1038/s41563-020-0729-1.

Correspondence and requests for materials should be addressed to Y.S.M. or B.L.

Reprints and permissions information is available at www.nature.com/reprints.

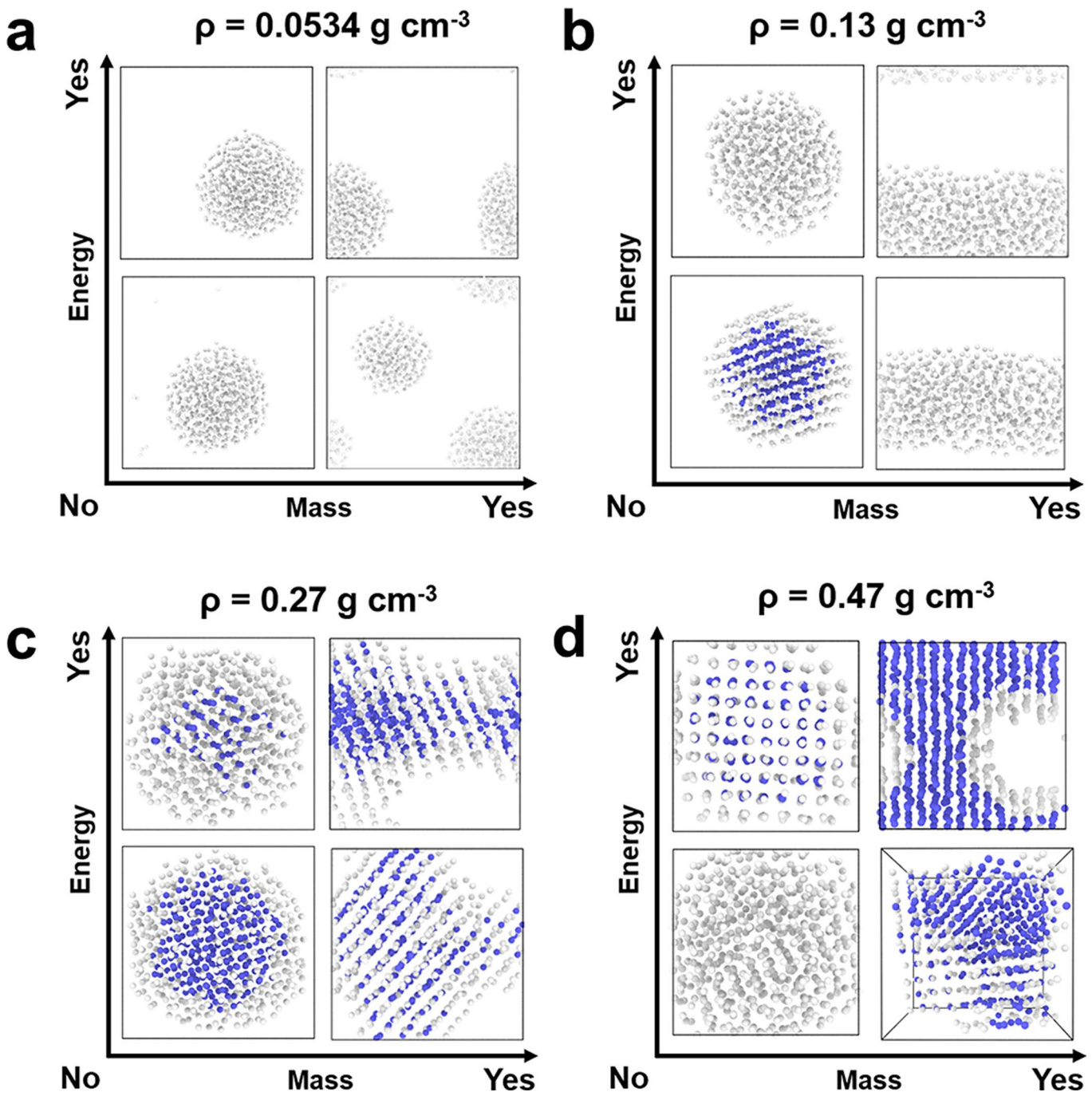

Extended Data Fig. 1 | Influence of local mass transport, energy transfer and current density (as represented by packing density) on the nucleation and phase transition of Li metal deposits by using ensembles of 600 Li atoms as the basis for the simulation. The packing density in a-d is 0.0534, 0.13, 0.27 and 0.47 g cm^{-3} respectively. The crystal structure (that is the *bcc* lattice) is represented in blue, whereas the amorphous fractions or phases in white or grey.

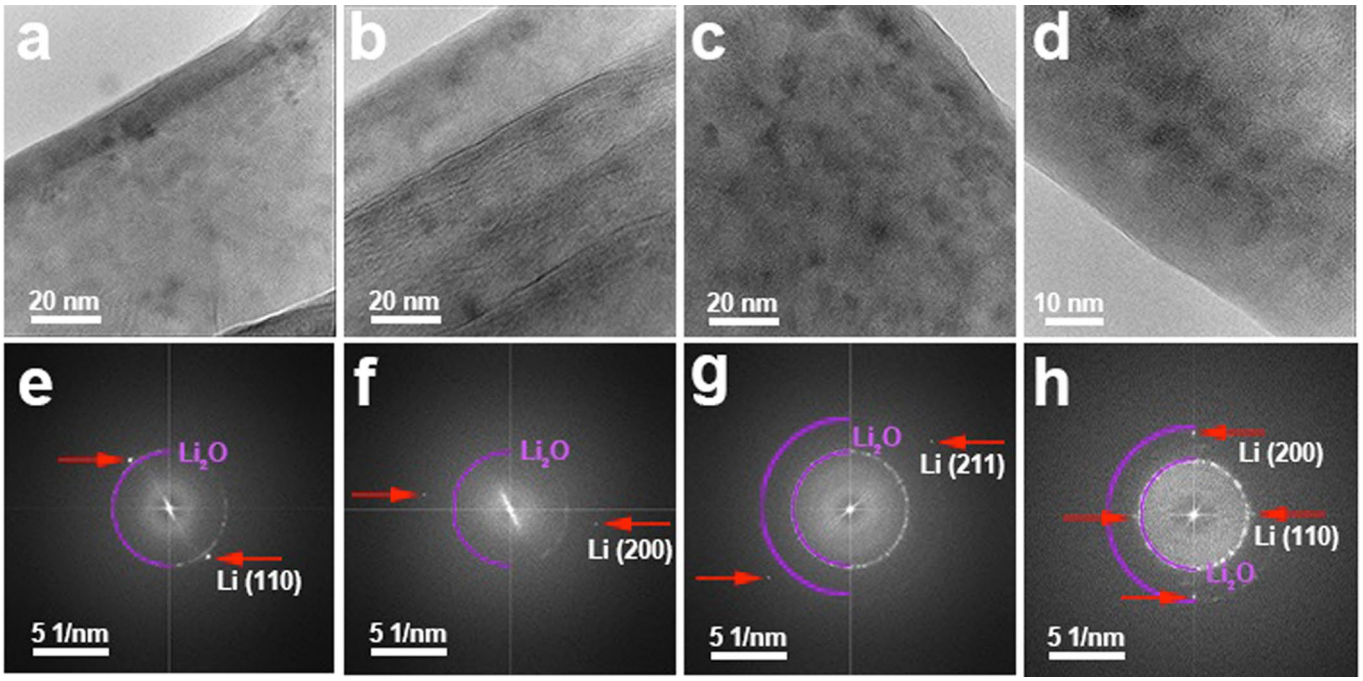

Extended Data Fig. 2 | Cryo-TEM images (**a-d**) and their FFT patterns (**e-h**) of Li deposits at 0.5 mA cm^{-2} for 2h. Besides (110) plane of Li metal, lattice fringes or FFT spots with lattice spacing of ~0.174 and ~0.142 nm was also observed, which belongs to the (200) and (211) planes of Li metal, respectively. Specially in d and h, both (200) and (110) planes of Li metal are present, which helps to determine the zone axis of [001] and confirm the phase of Li metal.

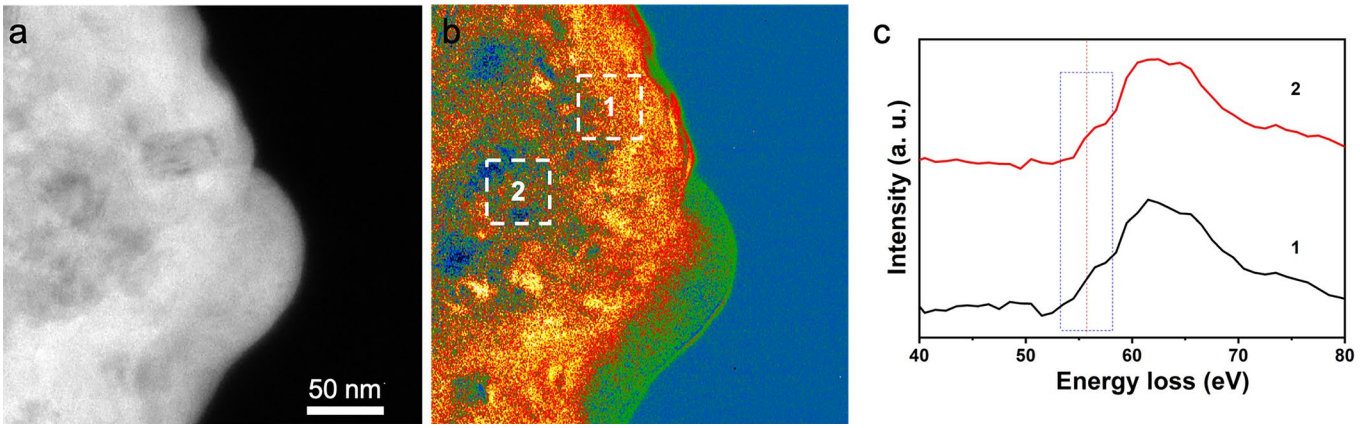

Extended Data Fig. 3 | Cryogenic STEM image (**a**), EELS Mapping (**b**) and spectra (**c**) of EDLi obtained at 0.5 mA cm^{-2} for 2h. The EELS mapping (**b**) is based on the intensity EELS spectra ranging from 53.5 eV to 58.5 eV (highlighted by the blue square in **c**), which contains the characteristic metallic/elemental Li K-edge threshold at about 55 eV. c presents the EELS spectra taken from Area 1 and Area 2 (labeled in **b**) representing the feature of highly crystalline Li and glassy Li respectively. Due to the presumed same SEI on the surface of Area 1 and Area 2, they show similar extended fine structure of Li K-edge after 60 eV. Both of them have the obvious characteristic metallic/elemental Li K-edge threshold at about 55 eV while the highly crystalline Li Area 1 shows a peak with slightly higher intensity than the glassy Li Area 2. This is reasonable due to the different degree of order/disorder structure in these two areas. It is worth to noting that it is difficult to obtain the higher-resolution STEM mapping due to the radiation damage caused by the high-energy beam used for STEM scanning even at cryogenic temperature.

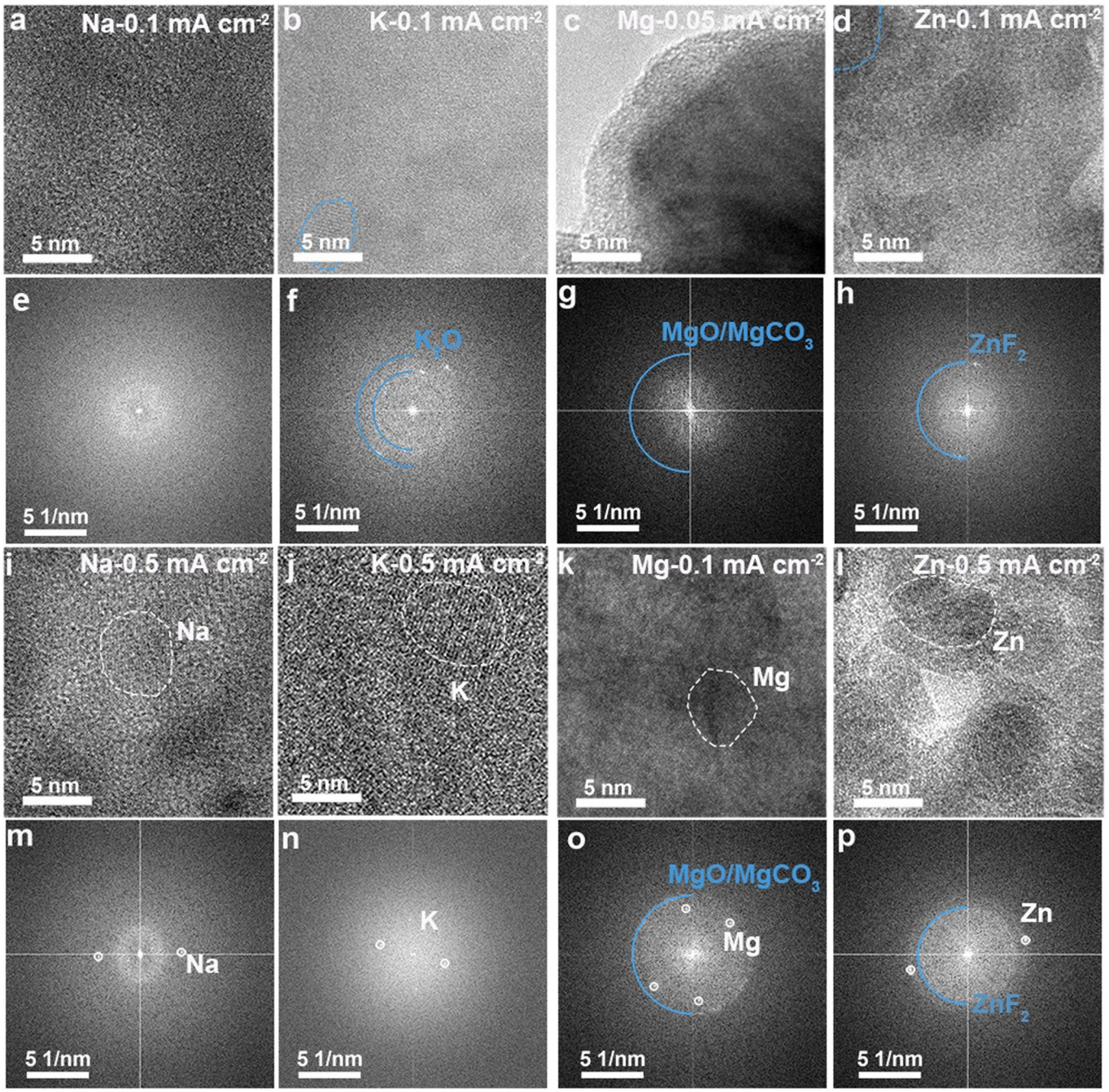

Extended Data Fig. 4 | Nanostructure evolution of Na, K, Mg and Zn deposits as a function of current density. TEM images (**a-d** and **i-l**) and the corresponding FFT patterns **(e-h** and **m-p**) of Na at 0.1 mA cm^{-2} (**a** and **e**) and 0.5 mA cm^{-2} (**i** and **m**), K at 0.1 mA cm^{-2} (**b** and **f**) and 0.5 mA cm^{-2} (**j** and **n**), Mg at 0.05 mA cm^{-2} (**c** and **g**) and 0.1 mA cm^{-2} (**k** and **o**) and Zn at 0.1 mA cm^{-2} (**d** and **h**) and 0.5 mA cm^{-2} (**l** and **p**). The crystalline portion of the Na, K, Mg, and Zn deposits are labeled by the white dash lines.